The Astronomical Journal, 171:108 (19pp), 2026 February https://doi.org/10.3847/1538-3881/ae2fb7

A Search for Late-type Brown Dwarfs in the Euclid Quick Data Release 1

Frank Kiwy[1], J. Davy Kirkpatrick[2], Adam C. Schneider[3], Aaron M. Meisner[4,5,6], Jacqueline K. Faherty[7], Marc J. Kuchner[8], Daniella Bardalez Gagliuffi[9], Sarah L. Casewell[10], Thomas P. Bickle[1,11], and The Backyard Worlds: Planet 9 Collaboration

[1] Backyard Worlds: Planet 9, USA
[2] IPAC, Mail Code 100–22, Caltech, 1200 E. California Blvd., Pasadena, CA 91125, USA
[3] United States Naval Observatory, Flagstaff Station, 10391, West Naval Observatory Rd., Flagstaff, AZ 86005, USA
[4] NSF National Optical-Infrared Astronomy Research Laboratory, 950 N. Cherry Ave., Tucson, AZ 85719, USA
[5] Carl and Lily Pforzheimer Foundation Fellow, Radcliffe Institute for Advanced Study at Harvard University, 10 Garden St., Cambridge, MA 02138, USA
[6] Center for Astrophysics | Harvard & Smithsonian, 60 Garden St., Cambridge, MA 02138, USA
[7] Department of Astrophysics, American Museum of Natural History, Central Park West at 79th St., NY 10024, USA
[8] Exoplanets and Stellar Astrophysics Laboratory, NASA Goddard Space Flight Center, 8800 Greenbelt Rd., Greenbelt, MD 20771, USA
[9] Department of Physics & Astronomy, Amherst College, 25 East Dr., Amherst, MA 01003, USA
[10] School of Physics and Astronomy, University of Leicester, University Rd., Leicester, LE1 7RH, UK
[11] School of Physical Sciences, The Open University, Milton Keynes, MK7 6AA, UK
Received 2025 November 5; revised 2025 December 15; accepted 2025 December 17; published 2026 January 23

Abstract

We present the identification and characterization of 15 mid-to-late T dwarf candidates in the Euclid Quick Release 1 (Q1) data set, based on a combined photometric and spectroscopic analysis. Candidates were initially selected via color-based cuts in the Euclid $Y_E - J_E$ and $J_E - H_E$ color–color space, targeting the region occupied by ultracool dwarfs (UCDs) in synthetic photometry from the A. Sanghi et al. sample. From an initial pool of 38,845 sources, we extracted low-resolution near-infrared spectra from the Euclid Near-Infrared Spectrometer and Photometer instrument and applied a two-stage validation procedure that included spectral template fitting followed by visual inspection. Eight of the 15 validated candidates are newly identified objects with no prior literature association. We examined their morphological and photometric properties, and compared them with established spectral standards. Photometric distances were derived using band-averaged distance modulus estimates. We discuss the limitations and promise of the Euclid survey for UCD studies, and demonstrate the potential for discovering substellar populations beyond the reach of current wide-field surveys.

Unified Astronomy Thesaurus concepts: Brown dwarfs (185); T dwarfs (1679); Near infrared astronomy (1093); Broad band photometry (184)

1. Introduction

Brown dwarfs occupy the range between the highest-mass giant planets and the lowest-mass stars, typically between ∼13 and 80 Jupiter masses, lacking the core temperatures necessary to sustain hydrogen fusion (W. B. Hubbard et al. 1997; A. Burrows et al. 2001; I. Baraffe et al. 2003; E. Moraux et al. 2003; D. S. Spiegel et al. 2011; S. B. Dieterich et al. 2018; N. Grieves et al. 2021). As a consequence, these substellar objects cool and fade over time, making their detection increasingly challenging at later evolutionary stages and lower masses (G. Chabrier et al. 2005; J. D. Kirkpatrick et al. 2012). The identification and characterization of brown dwarfs, particularly those of late spectral types (e.g., T and Y dwarfs), is essential for understanding the low-mass end of the initial mass function, substellar cooling rates, and the overall census of the solar neighborhood (K. L. Luhman et al. 2000; M. J. Huston & K. L. Luhman 2021; J. D. Kirkpatrick et al. 2021; W. M. J. Best et al. 2024; J. D. Kirkpatrick et al. 2024).

Large-scale photometric and spectroscopic surveys have greatly expanded the known population of brown dwarfs over the last few decades (e.g., M. C. Cushing et al. 2011; J. D. Kirkpatrick et al. 1999, 2021; J. D. Kirkpatrick et al. 2024). Ground-based efforts such as the Sloan Digital Sky Survey (SDSS; D. G. York et al. 2000), the Two Micron All Sky Survey (2MASS; R. M. Cutri et al. 2003; M. F. Skrutskie et al. 2006), the UKIRT Infrared Deep Sky Survey (UKIDSS; A. Lawrence et al. 2007), the VISTA Hemisphere Survey (VHS; R. G. McMahon et al. 2013), and the Panoramic Survey Telescope and Rapid Response System Survey (Pan-STARRS1; K. C. Chambers et al. 2016) have been instrumental in identifying large samples of L and early T dwarfs. Space-based missions like the Wide-field Infrared Survey Explorer (WISE; E. L. Wright et al. 2010) and Spitzer Space Telescope (Spitzer; M. W. Werner et al. 2004) extended this reach into the mid-infrared (MIR), enabling the discovery of even cooler objects, including late T and Y dwarfs. More recently, Gaia (Gaia Collaboration et al. 2016) has provided high-precision astrometry for brighter ultracool dwarfs (UCDs), while the James Webb Space Telescope (JWST; J. P. Gardner et al. 2006) has begun to probe the faintest and coldest members of the substellar population with unprecedented sensitivity and resolution (e.g., S. A. Beiler et al. 2024; K. N. Hainline et al. 2024; J. K. Faherty et al. 2024, 2025; A. Y. A. Chen et al. 2025). These recent studies demonstrate that the coldest objects continue to reveal new and unexpected aspects of substellar atmospheres and chemistry. Taken together, these surveys now provide a robust framework for classifying and characterizing brown dwarfs across a wide range of temperatures and masses.

The Euclid space telescope (R. J. Laureijs et al. 2010), although primarily designed for cosmology, offers a unique opportunity to identify faint brown dwarfs through its wide-field near-infrared (NIR) photometry and slitless spectroscopy. Its Near-Infrared Spectrometer and Photometer (NISP; Euclid Collaboration et al. 2025a) provides simultaneous Y_E, J_E, and H_E photometry along with low-resolution spectra ($R \simeq 500$) over a contiguous NIR range (1.2–1.9 μm), making it particularly suitable for detecting the broad absorption features characteristic of T-type atmospheres.

Our work complements several recent studies utilizing Euclid data. Notably, C. Dominguez-Tagle et al. (2025) and M. Žerjal et al. (2025) conducted spectroscopic and photometric searches for UCDs, respectively, while A. Mohandasan et al. (2025) spectroscopically identified UCDs in the Deep Field North, primarily of earlier spectral types. More recently, Z. Zhang & Y. Li (2025) used machine learning tools to photometrically identify 25 UCDs in the M and L regimes. In contrast, our study combines photometric selection with spectroscopic validation, focusing specifically on late-type brown dwarfs.

In this work, we present a search for mid-to-late T dwarfs in the Euclid Quick Release (Q1) dataset (Euclid Collaboration et al. 2025b). We begin with a photometric selection in the $Y_E - J_E$ versus $J_E - H_E$ color–color space to isolate potential candidates. These sources are then subjected to a two-stage validation process that combines automated spectral template fitting and manual inspection. A final sample of 15 high-confidence brown dwarf candidates is identified and analyzed in detail.

This paper is outlined as follows. In Section 2, we describe the color-based selection strategy. Section 3 details the spectroscopic validation of the candidates. The properties of the final sample are examined in Section 4, including comparisons with spectral standards. In Section 5, we propose refined selection criteria informed by our results. Section 6 discusses our findings in the context of previous studies, classification uncertainties, and the implications for future Euclid searches. Finally, we summarize our findings in Section 7.

2. Photometric Selection

To isolate candidate late-type brown dwarfs in the Euclid Q1 dataset, we focused on the three NIR filters Y_E, J_E, and H_E, which are particularly well suited for detecting mid-to-late T dwarfs.

These cool objects are significantly brighter in the infrared than at visual wavelengths, making the Euclid NISP bands ideal for their detection and characterization. In contrast, the Visual Imager (VIS; Euclid Collaboration et al. 2025c) is not well suited for this purpose: Late T dwarfs are intrinsically very faint at optical wavelengths, and are often undetected or detected at very low signal-to-noise ratio (S/N) in the VIS band, especially at the faint end of the Q1 sample. While some brighter late T dwarfs may be detected by VIS, relying on it would lead to incompleteness and potential selection biases.

To define our selection region, we used synthetic photometry from the A. Sanghi et al. (2024) sample of UCDs, spanning spectral types M6 to T9, and mapped their locations in the Euclid color–color space defined by $Y_E - J_E$ and $J_E - H_E$. The background distribution in Figure 1 shows the density of sources from the Euclid Q1 merged catalog (Euclid Collaboration et al. 2025d) with high-quality detections (`det_quality_flag = 0`) and positive fluxes in the Y_E, J_E, and H_E bands. Magnitudes were computed from the template-fit fluxes using the AB zero-point, and we imposed an upper magnitude limit of 23 mag in all bands to ensure good photometric reliability and minimize contamination from faint, low-S/N sources. None of the 15 candidates in our final sample approach this limit, with the faintest having $Y_E = 22.5$ mag.

The A. Sanghi et al. (2024) objects are shown in Figure 1 with a spectral-type color gradient. Mid-to-late T dwarfs clearly separate from earlier-type UCDs (late M, L, and early T) and from the bulk of the main stellar and galaxy loci. Based on this distribution, we adopted color constraints of $0.1 < Y_E - J_E < 0.9$ and $J_E - H_E < -0.1$, indicated by black dashed lines.

The application of these color and magnitude constraints to the Euclid Q1 dataset yielded an initial sample of 38,845 sources that were retained for further analysis.

3. Spectroscopic Validation

While the color-based photometric selection yields 38,845 potential sources, the vast majority are contaminants. To refine this sample, we employed a two-stage validation procedure that combined spectral template fitting with visual inspection.

In the first stage, we retrieved available spectra for each source from the ESA Euclid archive (European Space Agency & Euclid Consortium 2025) and compared them to standards defined by A. J. Burgasser et al. (2006), J. D. Kirkpatrick et al. (2010), and M. C. Cushing et al. (2011), as compiled by A. J. Burgasser & Splat Development Team (2017), covering spectral types from M0 to T9. Each Euclid spectrum was trimmed to the 1.22–1.88 μm range to avoid increased noise toward the spectral edges. We chose to exclude only pixels with zero flux values, and did not apply additional filtering based on the `MASK` (pixel mask), `QUALITY` (pixel quality flag), or `NDITH` (number of spectra used in combination) columns included in the spectrum FITS files. While more stringent filtering criteria are commonly employed, we found that such filtering may unnecessarily exclude data points that, despite minor calibration warnings, still provide useful information for spectral classification. A case in point is the spectrum of E0328−2749, shown in Figure 2, which yields a robust fit despite containing many flagged pixels (marked in orange). We therefore opted for a more inclusive approach to preserve potentially informative spectral features.

Nonetheless, we discarded any spectrum with a global S/N below 1.0 to ensure a minimum level of reliability in the fitting process.

Motivated by the inconsistent performance of the reduced chi-squared statistic on low-S/N Euclid spectra, we explored alternative similarity metrics for spectroscopic validation. We found that cosine similarity significantly outperforms the reduced chi-squared in suppressing false positives, by a factor of 3–4, particularly for low-S/N spectra, which are prevalent in our initial color-based photometric selection due to the intrinsic faintness of the targeted objects. While in some cases the reduced chi-squared yields slightly better spectral fits, we adopted cosine similarity for the spectroscopic candidate selection due to its superior robustness in noisy regimes. The use of the reduced chi-squared as a comparison metric is retained for the final spectral classification step.

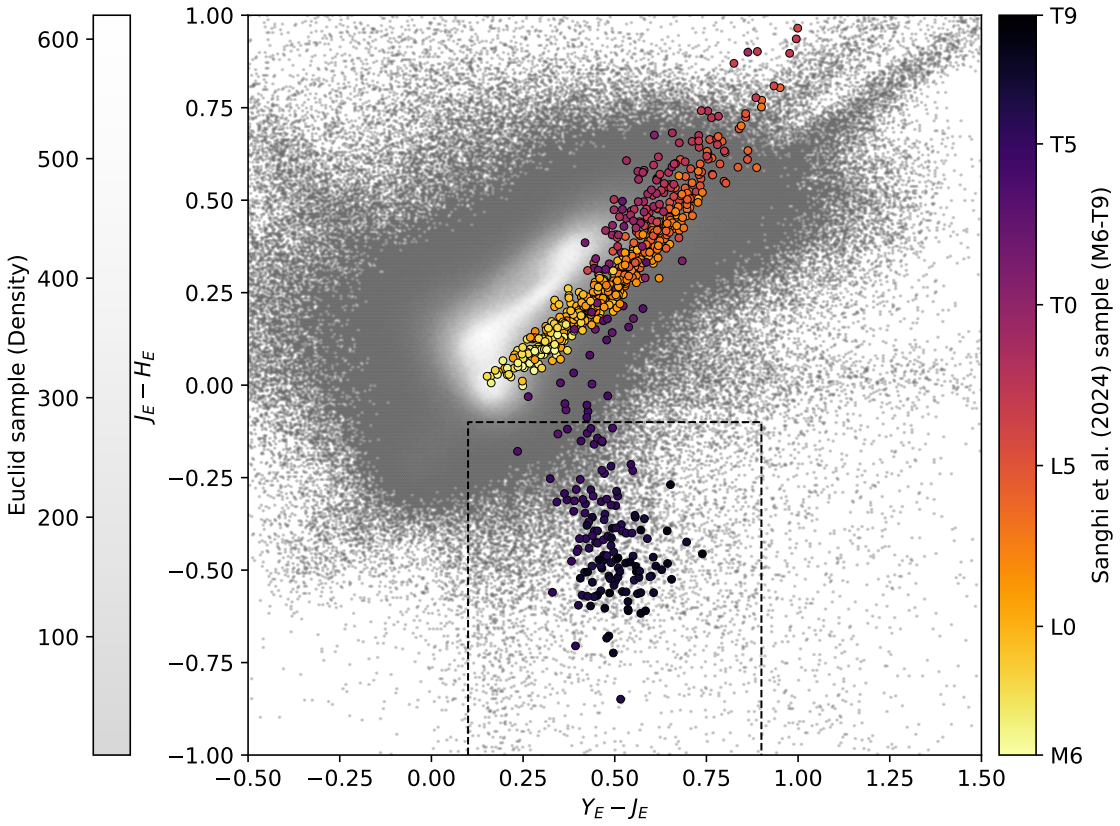

Figure 1. Color–color diagram showing the Euclid $Y_E - J_E$ vs. $J_E - H_E$ color space. The grayscale background represents the density of sources from the Euclid Q1 dataset, limited to high-quality detections and magnitudes brighter than 23 mag in all three bands. Overplotted are synthetic Euclid colors of M6–T9 UCDs from the A. Sanghi et al. (2024) sample, colored by spectral type. Mid-to-late T dwarfs clearly deviate from earlier-type UCDs, forming a distinct population toward redder $Y_E - J_E$ and bluer $J_E - H_E$ colors. The black dashed lines indicate the adopted color selection boundaries ($0.1 < Y_E - J_E < 0.9$ and $J_E - H_E < -0.1$) used to identify candidate mid-to-late T dwarfs in the Euclid Q1 dataset.

Cosine similarity has been successfully applied in other spectral classification contexts, for instance in M. Yang et al. (2024) or C. Viscasillas Vázquez et al. (2024). It measures the cosine of the angle between two nonzero vectors—here, the observed and template spectra. It is defined as the L2-normalized dot product:

$$k(A, B) = \frac{\langle A, B \rangle}{\|A\| \cdot \|B\|} = \frac{\sum_{i=1}^{n} A_i B_i}{\sqrt{\sum_{i=1}^{n} A_i^2} \cdot \sqrt{\sum_{i=1}^{n} B_i^2}}, \quad (1)$$

where A and B denote the flux values of the observed and template spectra, respectively. A value close to 1 indicates a strong match, corresponding to a small angle between the spectra in vector space.

Each Euclid spectrum was compared to the full grid of spectral templates using the cosine similarity metric. Sources whose best-matching template corresponded to a spectral type between T0 and T9 were flagged as potential candidates. This resulted in an initial selection of 453 sources for further analysis.

However, only 15 of these objects were ultimately classified as high-confidence brown dwarf candidates. This significant reduction is primarily due to the limitations of the Euclid NISP instrument and the low S/Ns of many extracted spectra. NISP is designed for broad cosmological objectives, such as galaxy redshift measurements and weak-lensing studies. Its resolving power of $R > 480$ (red grisms) for an object of $0\farcs5$ diameter is well suited for detecting broad emission features in distant galaxies, but not optimized for the identification of faint pointlike objects such as late-type brown dwarfs.

Moreover, the spectral quality for many sources in the Q1 release is modest, especially for fainter objects. The combination of low resolution, spectral artifacts, and noise often result in ambiguous or poorly constrained matches, even when the photometry is consistent with ultracool spectral types.

To address this, we performed a second-stage visual inspection of all fitted spectra and their associated template overlays. This step helped us eliminate sources with insufficient or poor signal in key diagnostic regions (e.g., CH_4 absorption at 1.3 and 1.6 μm).

This two-stage validation procedure was performed using `Euclid_tools` (F. Kiwy 2025), a Python package we developed to facilitate the analysis of Euclid data. The package provides tools for spectral extraction, template matching, and visual inspection, streamlining the process of identifying UCD candidates in large datasets like Euclid Q1.

After this rigorous vetting, only 15 sources were retained as robust, high-confidence mid-to-late T dwarf candidates. Eight of these sources are likely new discoveries, while the remaining seven have been previously reported in the literature (Table 1).

4. Candidate Analysis

4.1. Morphological and Photometric Properties

To evaluate the morphological properties and photometric reliability of the candidate sample, we examined several diagnostic parameters available in the Euclid Q1 merged

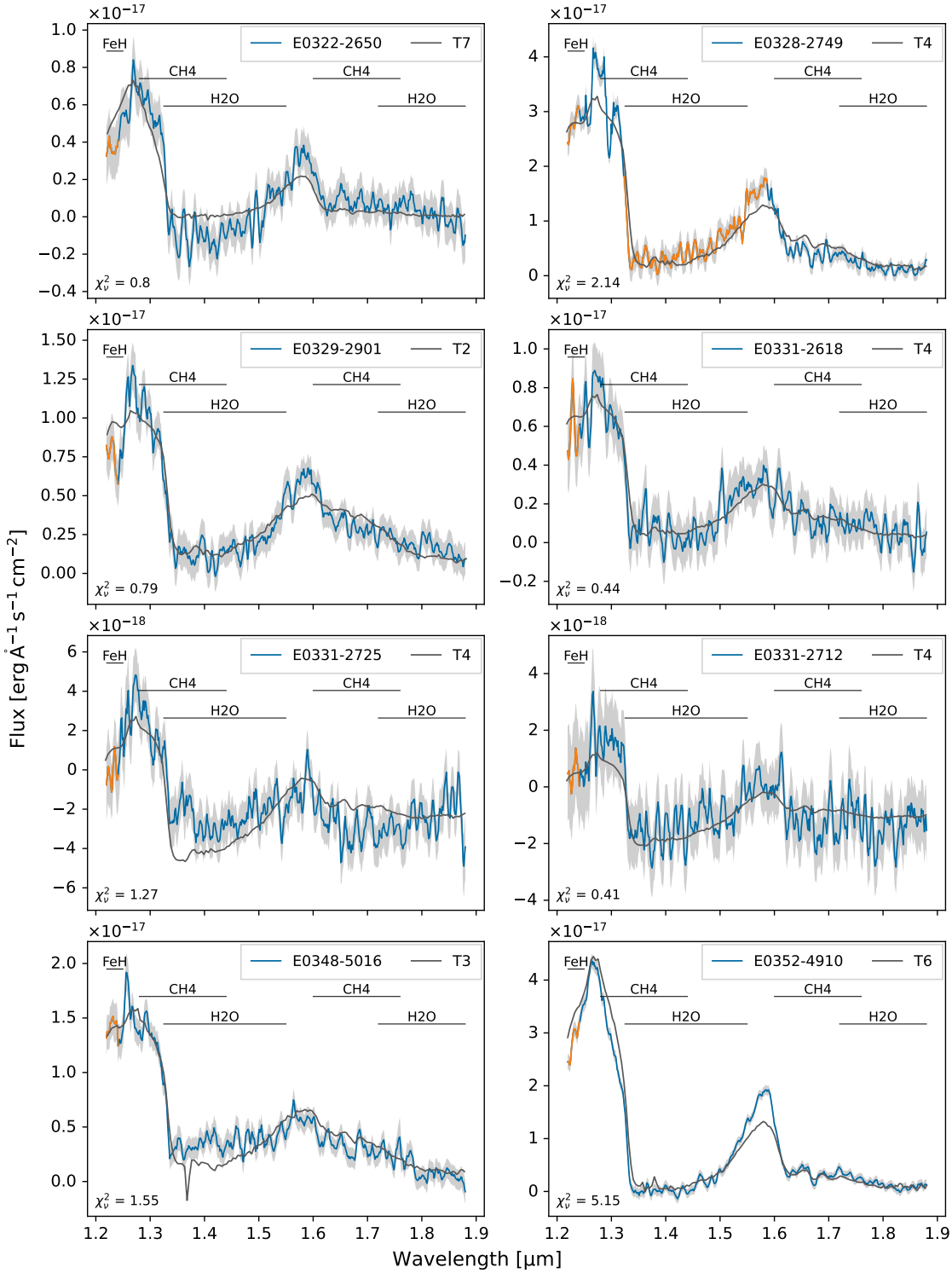

Figure 2. Comparison of smoothed candidate spectra (blue curves) with the Burgasser templates (dark gray curves) for the 15 selected candidates. The orange curves represent flagged values (e.g., due to low quality or artifacts). The shaded gray area around each spectrum represents the flux uncertainty. Key molecular absorption features are indicated by horizontal black lines (FeH, CH_4, and H_2O). Specifically, CH_4 bands span 1.28–1.44 μm in the J band and 1.6–1.76 μm in the H band; H_2O bands span 1.325–1.55 μm in the J band and 1.72–2.14 μm in the H band. While several spectra exhibit clear methane absorption features characteristic of mid-to-late T dwarfs (e.g., at 1.3 and 1.6 μm), others show considerable noise or deviations from the templates, reflecting the limitations of low-resolution slitless spectroscopy and varying data quality in the Euclid Q1 release. The reduced chi-squared fit statistic, displayed in the bottom-left corner, provides a quantitative measure of the fit quality.

catalog. Four classification-related fields—`blended_prob`, `variable_flag`, `binary_flag`, and `extended_prob`—are missing for all sources in our final sample and thus could not be used for quality assessment.

The `point_like_prob` parameter, which quantifies the likelihood that a source is pointlike, is only available for 10 of the 15 candidates. However, its values are consistently low (<0.5), suggesting nonstellar morphologies. This is likely an

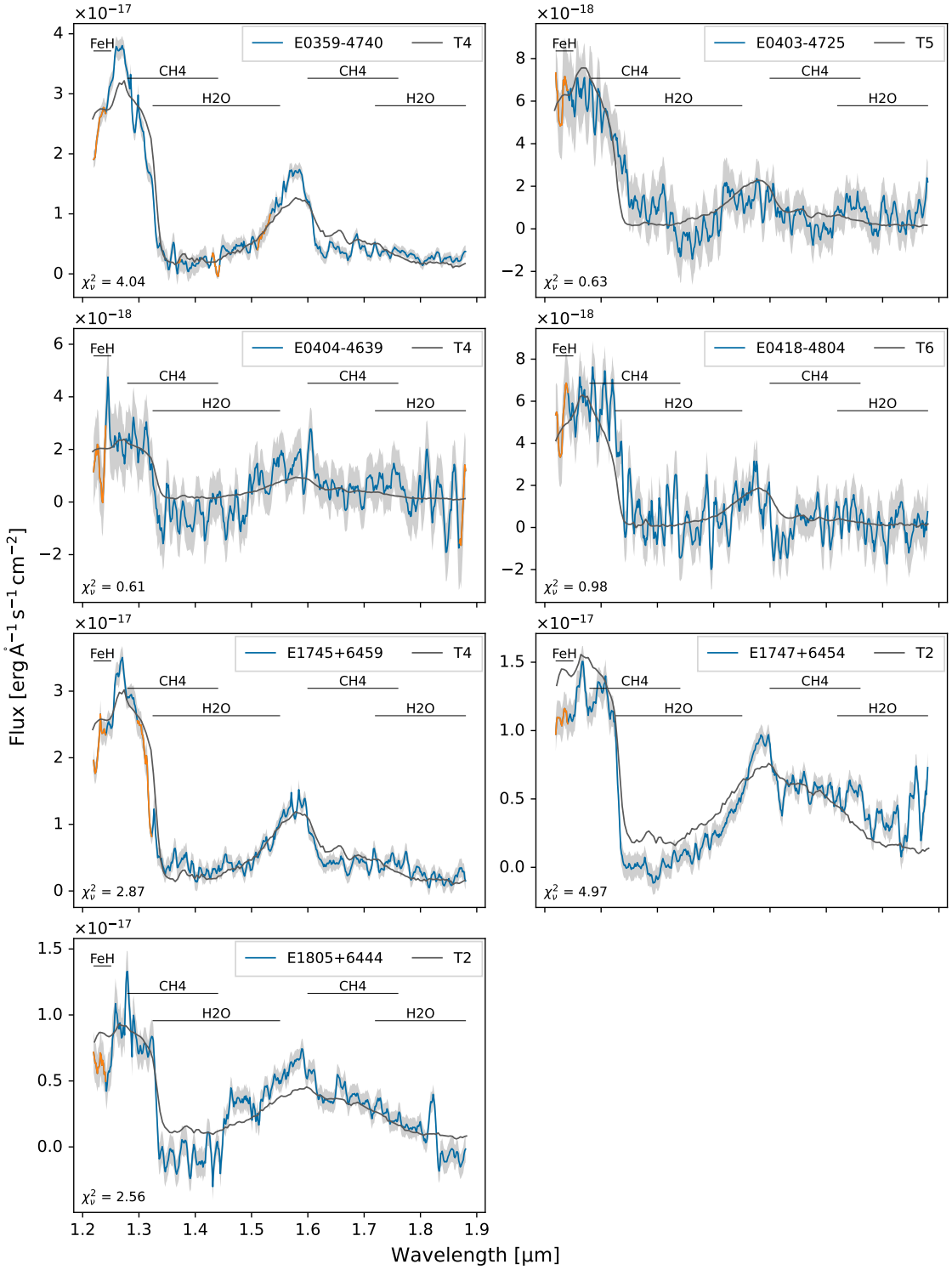

Figure 2. (Continued.)

artifact of the low S/Ns and NIR-only detection for faint objects such as mid-to-late T dwarfs. In several cases, visual inspection of the image cutouts reveals clearly pointlike profiles despite the low `point_like_prob`, indicating that this parameter is not fully reliable for faint brown dwarf candidates.

As a more robust alternative, we considered the `mumax_minus_mag` parameter, which is defined as the difference between the peak surface brightness (`mu_max`) and the total magnitude (`mag_stargal_sep`). This quantity, expressed in magnitudes per square arcsecond (mag arcsec^{-2}), serves as a proxy for the compactness of the source: Larger negative values typically correspond to more centrally concentrated (i.e., pointlike) objects. All candidates have valid entries for this parameter, and the values support the compact nature expected for brown dwarfs (Table 2).

The `fwhm` parameter provides the full width at half-maximum of the source, as used by `a-phot` to define

Table 1
Summary of the 15 High-confidence Mid-to-late T Dwarf Candidates Identified in This Work

Object Name	Short Name	Object ID	R.A. (deg)	Decl. (deg)	Lit. References	Lit. SpT
E032252.96−265010.92	E0322−2650	−507206654268363669	50.720665	−26.836367	⋯	⋯
E032759.32−274940.51	E0328−2749	−519971822278279190	51.997182	−27.827919	(2), (3)	T6, T6
E032925.80−290153.42	E0329−2901	−523574860290315045	52.357486	−29.031505	(2)	T4
E033117.79−261858.95	E0331−2618	−528241075263163744	52.824107	−26.316374	(2)	T5
E033118.45−272549.34	E0331−2725	−528268759274303728	52.826876	−27.430373	⋯	⋯
E033126.66−271240.56	E0331−2712	−528610966272112669	52.861097	−27.211267	⋯	⋯
E034825.35−501644.69	E0348−5016	−571056342502790814	57.105634	−50.279081	(3)	T
E035231.98−491058.81	E0352−4910	−581332495491830038	58.133249	−49.183004	(1), (2)	T7, T7
E035909.93−474057.42	E0359−4740	−597913643476826162	59.791364	−47.682616	(1), (2), (3)	T8, T7, T7
E040322.22−472516.51	E0403−4725	−608425655474212533	60.842566	−47.421253	⋯	⋯
E040417.08−463943.06	E0404−4639	−610711868466619603	61.071187	−46.661960	⋯	⋯
E041818.40−480412.44	E0418−4804	−645766530480701214	64.576653	−48.070121	⋯	⋯
E174556.40+645937.11	E1745+6459	2664850113649936423	266.485011	64.993642	(1), (2), (3), (4)	T7, T6, T6, T7
E174710.98+645429.83	E1747+6454	2667957458649082863	266.795746	64.908286	⋯	⋯
E180505.04+644407.85	E1805+6444	2712709955647355135	271.270996	64.735514	⋯	⋯

Note. The columns list the assigned object name, object short name, Euclid object identifier, equatorial coordinates (R.A., decl.; J2000), and relevant literature references. Spectral types from the literature (Lit. SpT) are indicated in the same order as the references. The spectral classifications in M. Žerjal et al. (2025) are those reported by C. Dominguez-Tagle et al. (2025). All candidates were selected based on NIR color criteria, spectral template fitting, and visual inspection of their Euclid NISP spectra.
References. (1) J. Y. Zhang et al. (2024); (2) C. Dominguez-Tagle et al. (2025); (3) M. Žerjal et al. (2025); (4) G. N. Mace et al. (2013).

photometric apertures. All candidates show `fwhm` values between 1.″17 and 1.″39, reinforcing their pointlike character.

Lastly, the `ellipticity` parameter quantifies the elongation of the source based on its minor-to-major axis ratio. The candidates show low ellipticity values overall, further supporting their classification as substellar sources.

Together, these parameters help establish the morphological integrity of the candidates and provide supporting evidence for their compact, pointlike nature—characteristics consistent with the expectations for distant brown dwarfs. `mumax_minus_mag`, `fwhm`, and `ellipticity` have been successfully used by M. Žerjal et al. (2025) to isolate pointlike objects in their photometric search for UCDs in the Euclid Q1 dataset.

Consistent with their compact morphology, the candidates exhibit faint NIR fluxes, with J_E-band magnitudes ranging from 19.44 to 21.95 mag, with a median of 20.67 mag and mean of 20.80 mag—values consistent with expectations for cool, distant brown dwarfs (Table 3). Photometric uncertainties are low across all NIR bands, with median values of 0.017 mag in Y_E, 0.014 mag in J_E, and 0.015 mag in H_E, enabling reliable color measurements.

VIS-band magnitudes, where available, range from 24.47 to 26.75 mag, with a median of 25.56 mag, and the corresponding flux-based S/N varies between 8.04 and 35.42, with a median of 21.08. This highlights the suppressed optical flux of T dwarfs, and supports our decision to exclude VIS photometry from the color-based selection.

In contrast, the NIR bands show significantly higher S/Ns. The median flux S/N values are 63.25 in Y_E, 74.90 in J_E, and 74.05 in H_E, with mean values of 57.37, 76.91, and 68.20, respectively. These consistently high S/N values across the NIR support the robustness of both the photometric colors and the extracted spectra.

Color indices further validate the T dwarf classification. The $Y_E - J_E$ color spans 0.219 to 0.571 mag (median 0.403 mag), while $J_E - H_E$ values range from –0.484 to –0.106 mag (median –0.303 mag), reflecting the strong methane absorption characteristic of T dwarf atmospheres.

Table 2
Morphological Parameters of the 15 Mid-to-late T Dwarf Candidates

Object Name	$P_{\rm point}$	$P_{\rm spur}$	$\mu_{\rm max} - m$ (mag arcsec^{-2})	FWHM (arcsec)	Ellipticity
E0322−2650	0.00	0.03	−1.94	1.27	0.45
E0328−2749	0.45	0.07	−2.85	1.29	0.04
E0329−2901	⋯	0.03	−1.23	1.35	0.05
E0331−2618	0.04	0.08	−2.97	1.17	0.13
E0331−2725	⋯	0.02	−1.25	1.39	0.33
E0331−2712	⋯	0.02	−1.35	1.25	0.09
E0348−5016	0.32	0.04	−2.83	1.29	0.15
E0352−4910	0.18	0.07	−2.61	1.24	0.19
E0359−4740	0.50	0.07	−2.90	1.25	0.05
E0403−4725	0.00	0.03	−2.34	1.26	0.15
E0404−4639	⋯	0.02	−1.34	1.25	0.04
E0418−4804	⋯	0.08	−1.06	1.23	0.05
E1745+6459	0.33	0.13	−2.75	1.28	0.03
E1747+6454	0.10	0.04	−2.51	1.24	0.49
E1805+6444	0.14	0.04	−2.63	1.25	0.21

Note. The columns list the object name, pointlike probability ($P_{\rm point}$), spurious probability ($P_{\rm spur}$), difference between peak surface brightness and total magnitude ($\mu_{\rm max} - m$) as a proxy for compactness, full width at half-maximum (FWHM) in arcseconds, and ellipticity. These parameters help assess the pointlike nature and reliability of the detections. Missing values are indicated by an ellipsis.

Table 4 summarizes the properties of the 15 high-confidence T dwarf candidates in our final sample. Their photometric and morphological characteristics are consistent with expectations for mid-to-late T spectral types.

4.2. Spectral Classification via Template Matching

To determine the spectral types of our candidate brown dwarfs, we compared their Euclid NISP spectra to two sets of empirical templates: (1) M, L, and T dwarf spectra from A. J. Burgasser & Splat Development Team 2017 (used in Section 3; hereafter Burgasser templates), and (2) L, T, and Y

Table 3
Photometric Properties of the 15 Mid-to-late T Dwarf Candidates

Object Name	VIS (mag)	$\sigma_{\rm VIS}$ (mag)	Y_E (mag)	σ_Y (mag)	J_E (mag)	σ_J (mag)	H_E (mag)	σ_H (mag)	$Y_E - J_E$ (mag)	σ_{Y-J} (mag)	$J_E - H_E$ (mag)	σ_{J-H} (mag)
E0322−2650	26.750	0.135	21.661	0.028	21.297	0.021	21.403	0.020	0.364	0.035	−0.106	0.029
E0328−2749	24.806	0.040	19.916	0.013	19.436	0.008	19.739	0.011	0.480	0.015	−0.303	0.014
E0329−2901	⋯	⋯	21.179	0.017	20.670	0.014	20.882	0.015	0.509	0.022	−0.212	0.021
E0331−2618	26.207	0.112	21.957	0.029	21.399	0.020	21.851	0.026	0.558	0.035	−0.452	0.033
E0331−2725	⋯	⋯	22.428	0.043	21.917	0.032	22.321	0.043	0.511	0.054	−0.404	0.054
E0331−2712	⋯	⋯	22.055	0.039	21.836	0.027	22.105	0.035	0.219	0.047	−0.269	0.044
E0348−5016	25.493	0.048	20.863	0.017	20.497	0.014	20.660	0.014	0.366	0.022	−0.163	0.020
E0352−4910	24.468	0.033	19.853	0.010	19.450	0.008	19.934	0.008	0.403	0.013	−0.484	0.011
E0359−4740	24.807	0.031	20.091	0.012	19.615	0.007	20.002	0.009	0.476	0.014	−0.387	0.011
E0403−4725	26.396	0.115	21.859	0.030	21.530	0.025	21.907	0.030	0.329	0.039	−0.377	0.039
E0404−4639	⋯	⋯	22.009	0.033	21.684	0.025	21.895	0.034	0.325	0.041	−0.211	0.042
E0418−4804	⋯	⋯	22.524	0.042	21.953	0.029	22.290	0.039	0.571	0.051	−0.337	0.049
E1745+6459	24.894	0.037	20.283	0.014	19.846	0.013	20.272	0.013	0.437	0.019	−0.426	0.018
E1747+6454	25.732	0.056	20.636	0.015	20.316	0.011	20.549	0.012	0.320	0.019	−0.233	0.016
E1805+6444	25.634	0.085	21.006	0.014	20.620	0.011	20.731	0.012	0.386	0.018	−0.111	0.016

Note. Columns list the object name, apparent magnitudes (VIS, Y_E, J_E, H_E), and their associated uncertainties ($\sigma_{\rm VIS}$, σ_Y, σ_J, σ_H) in the VIS and NISP bands. The table also includes the $Y_E - J_E$ and $J_E - H_E$ color indices, along with their uncertainties (σ_{Y-J}, σ_{J-H}), which are key diagnostics for T dwarf classification. Magnitudes are derived from template-fitting photometry in the NIR bands and point-spread function fitting photometry in the VIS band, and are given in the AB system. Missing VIS photometry is indicated by an ellipsis.

Table 4
Statistical Summary of the 15 Mid-to-late T Dwarf Candidates

Parameter	Min.	Max.	Median	Mean
VIS (mag)	24.468	26.750	25.563	25.519
$\sigma_{\rm VIS}$ (mag)	0.031	0.135	0.052	0.069
Y_E (mag)	19.853	22.524	21.179	21.221
σ_Y (mag)	0.010	0.043	0.017	0.024
J_H (mag)	19.436	21.953	20.670	20.804
σ_J (mag)	0.007	0.032	0.014	0.018
H_E (mag)	19.739	22.321	20.882	21.103
σ_H (mag)	0.008	0.043	0.015	0.021
$Y_E - J_E$ (mag)	0.219	0.571	0.403	0.417
$J_E - H_E$ (mag)	−0.484	−0.106	−0.303	−0.298
$S/N_{\rm flux}$VIS	8.040	35.420	21.075	20.800
$S/N_{\rm flux}Y_E$	25.190	103.660	63.250	57.372
$S/N_{\rm flux}J_E$	34.340	153.050	74.900	76.915
$S/N_{\rm flux}H_E$	25.000	137.200	74.050	68.204
$P_{\rm point}$	0.000	0.500	0.160	0.206
$P_{\rm spur}$	0.020	0.130	0.040	0.051
$\mu_{\rm max} - m$ (mag arcsec^{-2})	−2.970	−1.060	−2.510	−2.171
FWHM (arcsec)	1.170	1.390	1.250	1.267
Ellipticity	0.030	0.490	0.130	0.163
$S/N_{\rm spec}$	1.169	7.611	3.372	3.512
SpT_B	2.000	7.000	4.000	4.067
SpT_T	2.000	7.000	5.000	4.667
Mean $d_{\rm phot}$ (pc)	30.100	184.051	105.288	100.339
Median $d_{\rm phot}$ (pc)	30.269	185.439	99.174	99.440
s.d. $d_{\rm phot}$ (pc)	0.643	11.601	3.088	5.106

Note. Magnitudes are in the AB system, photometric uncertainties are denoted by σ, $Y_E - J_E$ and $J_E - H_E$ are color indices, and S/N values are reported from fluxes. $P_{\rm point}$ and $P_{\rm spur}$ are the probabilities of being pointlike or spurious detections, respectively. $\mu_{\rm max} - m$ is the difference between peak surface brightness and total magnitude. $S/N_{\rm spec}$ is the S/N from the Euclid spectra. SpT_B and SpT_T are numerical spectral types inferred from Burgasser and Theissen templates, respectively. The $d_{\rm phot}$ values given are the mean, median, and standard deviation (s.d.) of the photometric distance estimates derived from the Y_E, J_E, and H_E bands.

dwarf spectra from C. A. Theissen et al. (2022, hereafter Theissen templates). Each Euclid spectrum was trimmed to the 1.22–1.88 μm range to exclude low-S/N edges and then smoothed using a Savitzky–Golay filter with a window length of 11 and a polynomial order of 2, which reduces pixel-scale noise while preserving broad spectral features. Zero-flux values were masked to prevent spurious contributions to the chi-squared statistic during template fitting.

The template spectra were processed similarly, trimmed to the same wavelength range and interpolated onto the Euclid wavelength grid. Each template was then flux-scaled to match the Euclid spectrum by applying a normalization factor equal to the ratio of their mean fluxes over the trimmed interval. For each candidate, we computed reduced chi-squared (χ^2_ν) values across all templates in both libraries and identified the best-fitting template and its associated spectral type. χ^2_ν as employed here is defined as

$$\chi^2_\nu = \frac{1}{\nu}\sum_i \frac{(F_{{\rm o},i} - F_{{\rm t},i})^2}{\sigma^2_{{\rm o},i}}, \quad (2)$$

where $F_{{\rm o},i}$ and $F_{t,i}$ are the observed and scaled template fluxes at pixel i, $\sigma_{{\rm o},i}$ is the observed flux uncertainty, and ν is the number of degrees of freedom (number of data points minus number of fitted parameters).

Figure 2 as well as Figure 4 in Appendix B present the best-fitting empirical templates for each candidate, together with their spectral types, and highlight key molecular absorption features including CH_4, H_2O, K I, and FeH.

4.3. Spectral Evaluation of Candidates

T dwarfs are characterized by distinctive NIR spectral features dominated by strong molecular absorption bands, particularly from methane (CH_4) and water (H_2O). The presence of deep CH_4 absorption troughs near 1.3 μm, 1.6 μm, and 2.2 μm marks the transition from late L to T

Table 5
Photometric and Spectral Types with Photometric Distance Estimates for Our 15 Candidates

Object Name	Type				d_{phot}		
	PHO	S_B	S_T	ADP	Mean (pc)	Median (pc)	s.d. (pc)
E0322−2650	⋯	T7	T7	T7	66	68	5
E0328−2749	T8 field	T4	T5	T5	51	51	2
E0329−2901	T4 young	T2	T2	T2	112	107	11
E0331−2618	T5 young	T4	T5	T5	130	134	7
E0331−2725	T4 young	T4	T4	T4	184	185	12
E0331−2712	T5 field	T4	T5	T5	147	147	3
E0348−5016	⋯	T3	T4	T4	90	90	2
E0352−4910	T7 field	T6	T7	T7	30	30	1
E0359−4740	T8 field	T4	T5	T5	56	57	2
E0403−4725	T8 field	T5	T6	T6	107	107	1
E0404−4639	T5 field	T4	T5	T5	138	137	1
E0418−4804	T4 young	T6	T6	T6	134	128	9
E1745+6459	T8 field	T4	T5	T5	62	63	2
E1747+6454	T5 field	T2	T2	T2	93	86	11
E1805+6444	⋯	T2	T2	T2	105	99	9

Note. The columns list the photometric spectral type (PHO) inferred from NIR colors, the spectral types derived from Burgasser (S_B) and Theissen (S_T) templates, the adopted spectral type (ADP; mean of S_B and S_T) used for distance estimation, and the mean, median, and standard deviation of the photometric distances (in parsecs). Photometric types are not provided for candidates with unreliable classifications (e.g., edge cases such as T9). Objects labeled as "young" reflect the outcome of the nearest-neighbor classification and should not be interpreted as evidence of confirmed youth.

spectral types (A. J. Burgasser et al. 2002). Within the Euclid NISP spectral wavelength range (1.2–1.9 μm, red grisms), the most prominent diagnostics are the suppressed H-band flux due to methane absorption and a peaked J band, with minimal flux in between. These features enable spectral classification even at low resolution, provided the S/N is sufficient. However, some brown dwarf candidates lie near the detection limit of the instrument, leading to noisy or incomplete spectra. In addition, variations in metallicity may lead to imperfect template fits, since the standard templates do not cover a range of metallicities for each spectral type. These limitations must be considered when assessing spectral fits.

In Appendix A, we present detailed evaluations of the spectra of our 15 candidate brown dwarfs, highlighting the characteristic NIR features used for their classification and noting cases where low S/N affects the spectral assessment.

4.4. Photometric Type and Distance Estimations

To complement the spectral classification, we estimated a photometric spectral type for each candidate based on its Euclid NIR colors. Using empirical polynomial relations published by A. Sanghi et al. (2024), we computed synthetic absolute magnitudes in the Euclid NISP Y_E, J_E, and H_E bands, separately for field-age and young objects. For each spectral type, we also derived color indices ($Y_E - J_E$, $Y_E - H_E$, and $J_E - H_E$), capturing characteristic trends across the M, L, and T dwarf sequence. Table 7 lists the resulting absolute magnitudes and colors, which form the basis for our photometric type and distance estimates.

A two-dimensional nearest-neighbor search was then performed in color–color space ($Y_E - J_E$ versus $J_E - H_E$) using a k-nearest-neighbor classifier with Euclidean distance as the metric. For each candidate, we identified the closest color match within the reference grid, along with its spectral type and associated fit statistic. To mitigate boundary effects, we excluded edge cases—specifically T9 classifications—whenever their nearest-neighbor distance exceeded two spectral subtypes.

In several cases, noticeable discrepancies arise between the photometric spectral types and those derived from template matching (see Table 5); for example, E0328–2749, E0359–4740, and E1745+6459 differ by up to four subtypes from the spectral types inferred using the Burgasser templates. This mismatch likely reflects the intrinsic color degeneracy of the late-T regime, where NIR colors do not follow a strictly linear trend with spectral type (see color–spectral type relations in Table 7).

Because our distance estimates rely on spectral types from template fitting, we also examined the consistency between the two template libraries. The spectral types obtained from the Theissen templates are broadly consistent with those inferred from the Burgasser templates, typically agreeing within one subtype. We therefore adopted the mean of the two classifications as the final spectral type for each source, which then served as the basis for photometric distance estimation.

Using these adopted spectral types, we inferred absolute magnitudes in the Euclid Y_E, J_E, and H_E bands from the empirical relations of A. Sanghi et al. (2024). From these and the observed apparent magnitudes, we computed individual band-specific photometric distances via the distance modulus (Table 5). We report both the mean and median of the three distances as the final estimate, while the dispersion among them was used as an estimate of the uncertainty. This approach provides consistent distance estimates in the absence of parallaxes while accounting for band-to-band variation and photometric noise.

4.5. Visual Inspection of Candidates

Each of the 15 brown dwarf candidates was visually inspected using $20'' \times 20''$ Euclid cutouts (Figure 3) in the VIS, Y_E, J_E, and H_E bands, together with a color composite where H_E, Y_E, and VIS are mapped to the red, green, and blue channels, respectively. All candidates are clearly detected in the NIR Y_E, J_E, and H_E bands, while VIS-band detections are generally faint, with some sources barely discernible—consistent with the intrinsically low optical fluxes of mid-to-late T dwarfs. Most objects appear compact and symmetric, with no significant signs of elongation or blending. A few lie in moderately crowded fields, where faint neighboring sources could influence aperture photometry or contaminate the extracted spectra. Overall, the majority of candidates exhibit isolated, pointlike morphologies, supporting the reliability of both their photometric and spectroscopic measurements.

In the following, we highlight noteworthy cases, focusing on potential blending or crowding issues that may affect the robustness of the photometry or spectra.

E0322−2650. Two overlapping bright sources (a star and a galaxy) are located to the left of the candidate, but they are sufficiently distant to avoid contaminating its photometry or spectrum.

E0331−2618. A nearby source lies approximately $1''$ to the upper left, potentially introducing slight contamination in the photometry or spectrum.

E0348−5016. Two faint neighboring sources are visible within $\sim 2''$ (top left and right), but are unlikely to affect the

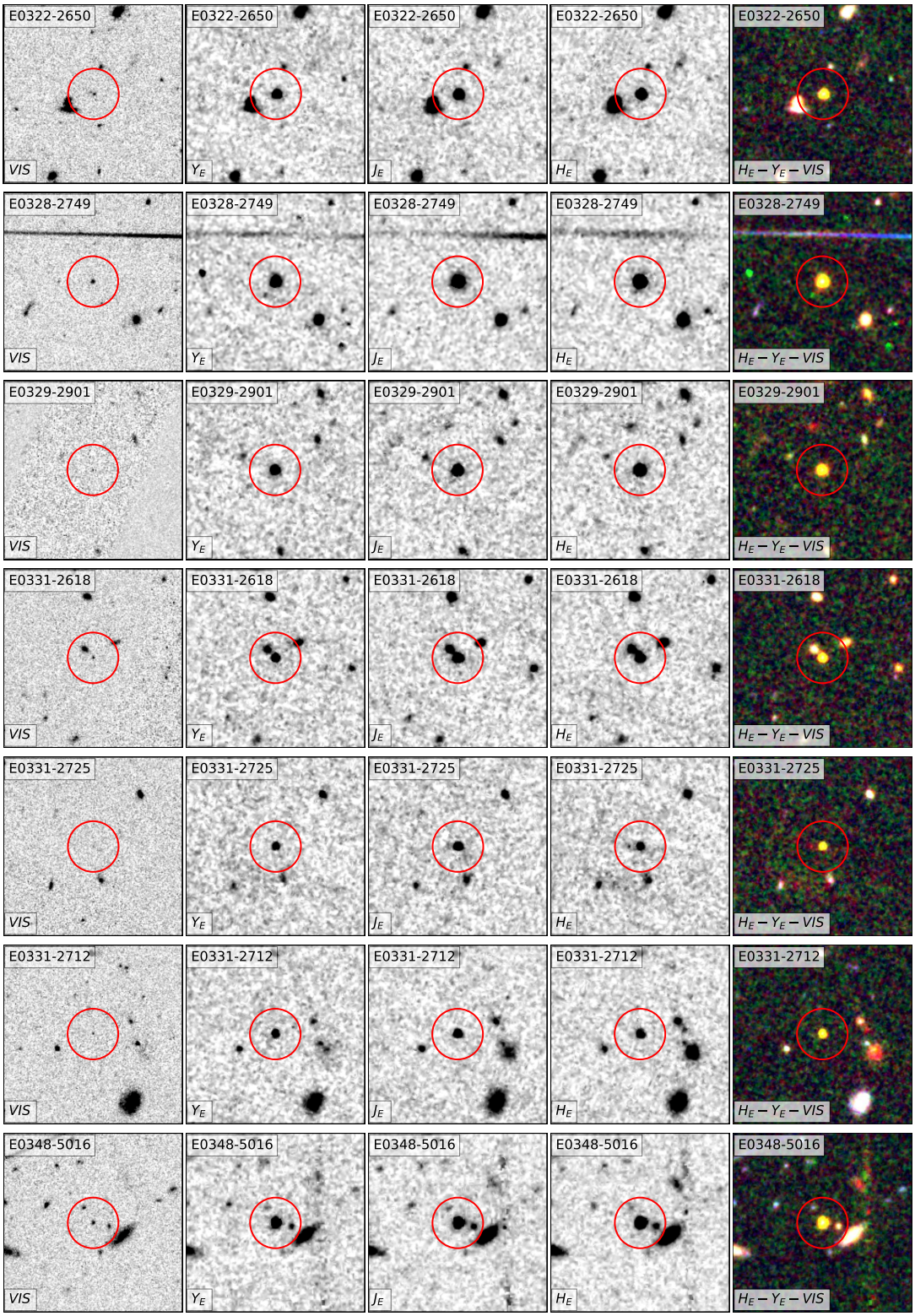

Figure 3. Euclid 20″ × 20″ cutouts of the 15 brown dwarf candidates in four bands, VIS, Y_E, J_E, H_E, and a color composite (left to right). Each candidate is centered within the red circle. The VIS cutouts illustrate that most candidates are barely detected at optical wavelengths, as expected for mid-to-late T dwarfs. In contrast, the majority are clearly visible in the Y_E, J_E, and H_E bands. Although most candidates appear compact and isolated, some might be slightly blended by nearby background sources. All images are oriented with north up and east to the left.

flux due to their faintness. A brighter galaxy lies ∼4″ to the bottom right, but its separation suggests a negligible impact on the candidate's photometry.

E0352−4910. The candidate nearly overlaps two very faint background objects, whose contribution to the total flux is likely minimal. Despite this, the spectrum is the cleanest in the sample and supports a high-confidence T6 classification, though a T7 match is also plausible depending on the band. This minor discrepancy could be attributed to residual flux from the background sources. Two additional faint sources are

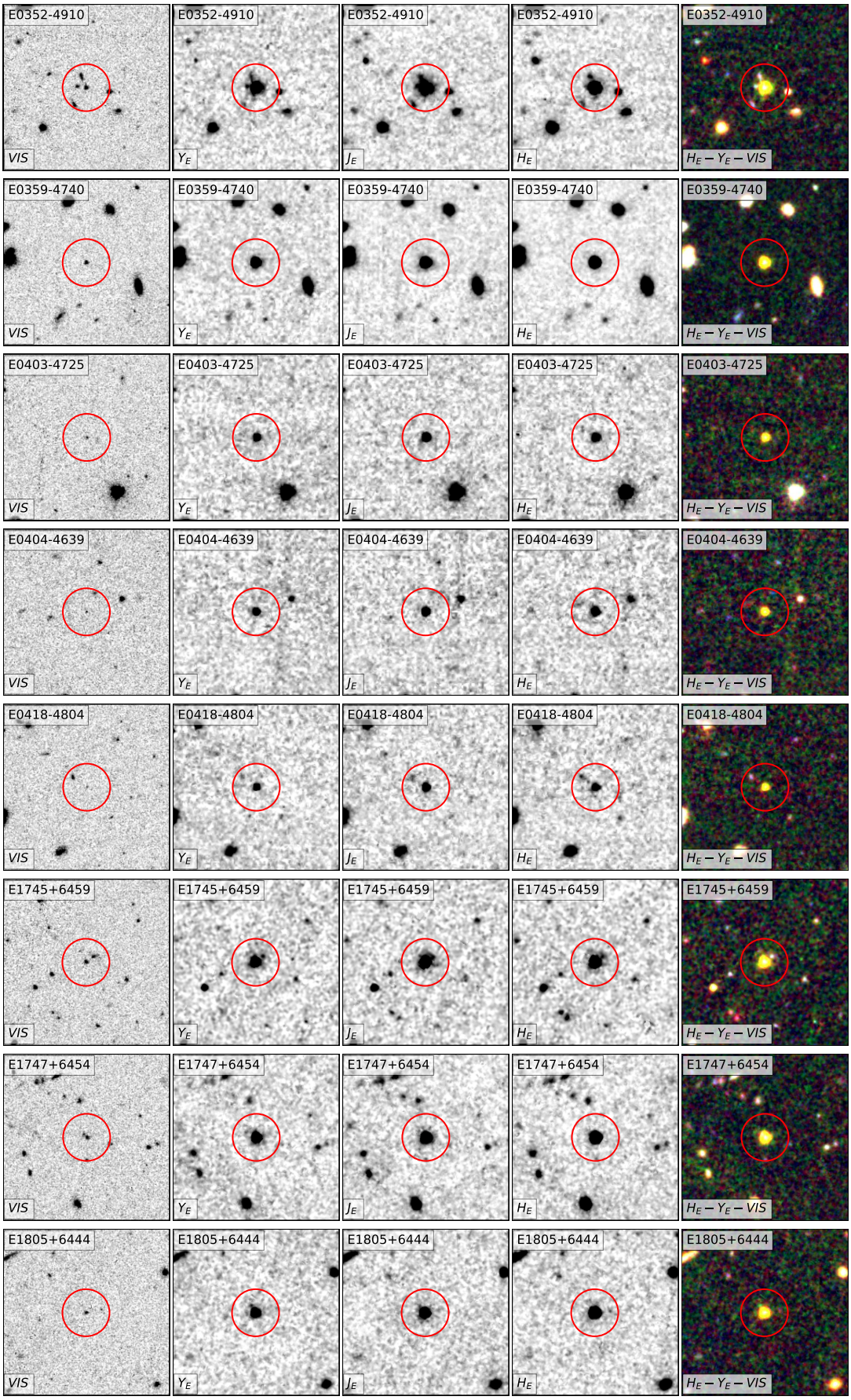

Figure 3. (Continued.)

Table 6
Refined Selection Criteria for the Euclid Q1 Merged Catalog

Parameter	Criterion
det_quality_flag	=0
spurious_prob	<0.2
ellipticity	<0.5
mumax_minus_mag	−3.1 to −0.9 mag arcsec^{-2}
fwhm	1.″0 to 1.″5
flux_y_templfit	>0
flux_j_templfit	>0
flux_h_templfit	>0
S/N Y_E	>24
S/N J_E	>32
S/N H_E	>24
Y_E, J_E, H_E	<23.0 mag
$Y_E - J_E$	0.1 to 0.9
$J_E - H_E$	<–0.1

Note. Magnitudes are computed in the AB system as $m = -2.5\log_{10}(f) + 23.9$, where f is the flux in microjansky (μJy).

located ∼4″ away (left and bottom left), but do not appear to affect the observed flux.

E1745+6459. A faint source is present within 1–2″ (top right), which may contribute slight contamination. However, the candidate's spectrum appears clean and well matched, supporting a confident classification.

4.6. Detections in Other Surveys

We searched for detections of our candidates in relevant previous NIR and MIR surveys and found that 11 sources have valid photometry in either VHS or the VISTA Kilo-degree Infrared Galaxy Survey (VIKING; A. Edge et al. 2013), including five detected only in the J band. Six candidates also have MIR counterparts in CatWISE2020 (F. Marocco et al. 2021). The combined photometry from these surveys is reported in Table 8, along with W1 − W2 colors and inferred photometric spectral types, which are broadly consistent with our adopted classifications. Magnitudes in this table are reported on the Vega system, in contrast to the AB system used for Euclid photometry throughout this paper.

5. Refinement of Photometric Selection

The initial candidate selection targeted mid-to-late T dwarfs in the Euclid Q1 merged catalog by applying basic photometric constraints based on expected NIR colors. Specifically, we required reliable flux measurements in the Y_E, J_E, and H_E bands, a magnitude cut of < 23 mag in each band to ensure reasonable S/N, and characteristic color ranges of $0.1 < Y_E - J_E < 0.9$ and $J_E - H_E < -0.1$. This yielded a preliminary sample of 38,845 sources.

To improve sample purity and reduce contamination, we applied additional criteria based on photometric and morphological quality indicators derived from our statistical analysis of confirmed candidates in Section 4.1. This included cuts on spurious detection probability (<0.2), ellipticity (<0.5), compactness index ($\mu_{\rm max} - m$ between −3.1 and −0.9 mag arcsec^{-2}), and FWHM (between 1.″0 and 1.″5). Additionally, we imposed minimum S/N thresholds in each band of $S/N_Y > 24$, $S/N_J > 32$, and $S/N_H > 24$. After applying these refined constraints, the sample was reduced to a cleaner and more manageable set of 11,302 photometric candidates, while retaining all 15 spectroscopically identified mid-to-late T dwarfs. Table 6 lists the complete morphological and photometric selection criteria applied to the Euclid Q1 merged catalog.

6. Discussion

The results presented in this work demonstrate the capability of the Euclid mission to identify and characterize brown dwarfs, despite its primary design for extragalactic cosmology. The combination of NIR imaging and slitless spectroscopy from the NISP instrument proves effective for detecting key features such as CH_4 and H_2O absorption, which are diagnostic of mid-to-late T dwarfs.

6.1. Comparison with Related Euclid-based Studies

Our study complements recent efforts based on Euclid Q1 data, particularly the spectroscopic analysis of UCDs by C. Dominguez-Tagle et al. (2025), the photometric selection conducted by M. Žerjal et al. (2025), and the spectroscopic work in the Euclid Deep Field North by A. Mohandasan et al. (2025). A key difference lies in the methodological design: C. Dominguez-Tagle et al. (2025) perform a purely spectroscopic search, identifying and classifying UCDs directly from the NISP spectral archive, whereas M. Žerjal et al. (2025) employ a purely photometric approach, relying on optical and NIR color cuts—most notably a VIS − $Y_E > 2.5$ criterion—to isolate high-purity UCD candidates. A. Mohandasan et al. (2025), in turn, use Euclid slitless spectroscopy to identify 33 new UCDs in the Deep Field North, primarily spanning spectral types M7 to T1 and J_E magnitudes of 17–21.

In contrast, our study adopts a hybrid approach that combines NIR color selection with subsequent spectroscopic validation, leveraging both photometric and spectroscopic information in an integrated framework. Unlike M. Žerjal et al. (2025), we do not require detections in the VIS band, allowing us to probe a fainter and potentially more complete population of late-type brown dwarfs, including sources that are undetected in optical wavelengths. Our methodology is optimized for the recovery of high-confidence mid-to-late T dwarfs, whereas the aforementioned studies target a broader UCD population. As such, our results serve as a complementary probe of the T dwarf population within the Euclid Q1 release, bridging the gap between the purely photometric and spectroscopic approaches adopted by other teams.

6.2. Spectral Classification and Uncertainties

Despite the use of two different template libraries (Burgasser and Theissen) enabling cross-validation of spectral classifications, the low spectral resolution and the relatively low S/N of many Euclid spectra impose limitations on the accuracy of subtype assignments, especially at the faint end.

However, even for objects with adequate S/N, discrepancies persist. For instance, some of the nearest objects in our sample (e.g., E0328−2749, E0359−4740, E1745+6459) exhibit elevated fluxes in the J- and H-band peaks, while others (e.g., E0329−2901, E1747+6454, E1805+6444) show stronger FeH absorption than their best-fit templates. These differences are likely the result of genuine astrophysical diversity among cool brown dwarfs. Variations in metallicity (e.g., I. S. McLean et al. 2003, 2007; A. J. Burgasser et al. 2006, 2025), surface gravity (e.g., M. R. Line et al. 2015, 2017; E. C. Martin et al. 2017), or

atmospheric chemistry and dynamics (e.g., M. C. Cushing et al. 2008; A. J. Burgasser et al. 2010b; M. S. Marley et al. 2010; G. Suárez et al. 2025) can significantly alter the depth and shape of key absorption bands (e.g., H_2O and CH_4), as well as the overall NIR continuum, leading to spectra that deviate from the solar-metallicity, field-gravity objects that define most existing templates. Additionally, unresolved multiplicity (e.g., L+T or T+Y systems) can produce blended spectral morphologies that mimic intermediate types or dilute characteristic features (e.g., A. J. Burgasser 2007; A. J. Burgasser et al. 2010a). Nonequilibrium chemistry (e.g., I. Yamamura et al. 2010; K. J. Zahnle & M. S. Marley 2014; B. E. Miles et al. 2020; S. K. Turner et al. 2025), driven by vertical mixing, can further modify the relative strengths of CH_4 and CO bands, while atmospheric heterogeneities or rotationally modulated variability (e.g., E. Buenzli et al. 2012; J. Radigan et al. 2012; S. A. Metchev et al. 2015; J. M. Vos et al. 2023; X. Chen et al. 2024) can lead to spectral shapes not well represented in static templates. These effects are compounded by the fact that the current T dwarf standards are sparse, heterogeneous in origin, and do not fully sample the parameter space of gravity, metallicity, cloud properties, or atmospheric dynamics. As a result, some of our T dwarfs likely fall outside the empirical distribution spanned by the standards themselves, leading to imperfect or ambiguous template matches even when the observational data are of good quality.

We also note that discrepancies between photometric and spectroscopic spectral types—sometimes spanning several subtypes—can arise from color degeneracies, spectral peculiarities, contamination from nearby sources, or differences in wavelength coverage (photometry: 950–2020 nm; spectroscopy, red grisms: 1206–1892 nm). Follow-up spectroscopy at higher resolution will be necessary to refine the classifications and investigate any outliers.

While our classification procedure yields results broadly consistent with expectations from colors and spectral morphology, several candidates exhibit differences compared to previously published spectral types. For example, E0328−2749 is classified as T5 in our analysis versus T6 in C. Dominguez-Tagle et al. (2025); E0329−2901 is assigned T2 compared to a literature type of T4; E0359−4740 is classified as T5 versus T7 in the literature; and E1745+6459 is assigned T5 compared to T6 reported by C. Dominguez-Tagle et al. (2025). These differences are most likely the result of variations in the spectral classification methodology. Factors such as the choice of template library, the spectral similarity metric employed, the treatment of masked or flagged spectral regions, and the rules used to reconcile conflicting spectral types can all influence the final classification. Nonetheless, the offsets remain within 1–2 subtypes and do not affect the interpretation of these sources as mid-to-late T dwarfs.

To assess the influence of flagged spectral regions on the classifications, we repeated the template fitting after removing all flagged pixels from the Euclid spectra. For all 15 candidates, including E0328−2749, which exhibits the largest contiguous region of flagged pixels (1.3–1.6 μm), the inferred spectral types remain unchanged. This indicates that for the objects in our sample the presence of flagged pixels does not influence the resulting classifications. We note that the impact of flagged regions will generally depend on the wavelength range and diagnostic features affected, and larger or strategically placed gaps could influence classifications in other cases.

6.3. Implications for Brown Dwarf Census

The identification of 15 high-confidence T dwarfs in just a fraction of the sky suggests that Euclid has strong potential to expand the census of substellar objects. The Euclid Q1 release covers 63.1 deg^2 of the Euclid Deep Fields, compared to the ∼14,500 deg^2 planned for the Euclid Wide Survey. Scaling our findings to this full area implies a potential yield of ∼3450 mid-to-late T dwarf candidates using our methodology. This estimate indicates that Euclid has the potential to increase the known mid-to-late T dwarf population by several thousand objects, enabling stronger statistical constraints on the substellar mass function and improving our understanding of their spatial distribution and kinematics. This expanded census will provide valuable insights into the formation and evolution of substellar objects across diverse Galactic environments, and offer a critical foundation for future studies of atmospheric diversity and chemical composition in the coldest brown dwarfs.

6.4. Outlook and Future Work

This study lays the groundwork for future brown dwarf searches in Euclid data releases. The forthcoming Data Release 1, scheduled for October 2026, will cover approximately 1900 deg^2 of sky—about 30 times the area of Q1. Applying our methodology to this dataset could yield on the order of 450 additional mid-to-late T dwarfs.

Follow-up spectroscopy of the current sample at higher S/N will be essential to refine spectral classifications, assess atmospheric properties, and confirm potential peculiarities such as low metallicity or unresolved binarity.

7. Conclusions

We have conducted a targeted search for late-type brown dwarfs in the Euclid Q1 dataset by combining photometric selection with spectral template matching. Starting from an initial sample of 38,845 color-selected sources, we employed a two-stage validation process that included spectral comparison to empirical templates and visual inspection of key diagnostic features. This approach led to the identification of 15 high-confidence T dwarf candidates, spanning spectral types from T2 to T7.

Each candidate was analyzed in detail, including assessments of morphological and photometric consistency, spectral fit quality, and the local imaging context to rule out contamination. Spectral types were assigned from high-confidence matches to two template libraries, with the mean value adopted as the final spectral type.

Photometric distances were derived for each candidate using synthetic magnitudes from the A. Sanghi et al. (2024) sample, yielding distances in the range of ∼30 to 185 pc. Eight of the 15 candidates in our sample appear to be previously unreported objects, whereas the remaining seven are consistent with known brown dwarfs in the literature.

This study demonstrates that Euclid, despite being optimized for cosmology, can contribute significantly to the study of UCDs. Our results highlight the potential of combining color selection and low-resolution NIR spectroscopy to robustly identify and characterize brown dwarfs in large survey data. Future data releases, with increased sky coverage and deeper sensitivity, are expected to substantially expand the known census of substellar objects.

Acknowledgments

This work is based on observations made with the Euclid space telescope, a European Space Agency (ESA) mission with contributions from NASA and the Euclid Consortium. We acknowledge the use of data from the Euclid Quick Release 1 (Q1), publicly available through the ESA Euclid Science Archive (European Space Agency & Euclid Consortium 2025). We thank the Euclid Consortium for their efforts in the design, construction, and data processing of the mission, and the ESA Science Data Centre (ESDC) for providing access to the Q1 merged catalog and spectral products. We also recognize the Euclid Science Ground Segment (SGS) for their contributions to data processing and quality assessment, which enabled this analysis. This work makes use of data products from the VISTA Hemisphere Survey (VHS) and the VISTA Kilo-degree Infrared Galaxy (VIKING) Survey, obtained with the VIRCAM instrument on the Visible and Infrared Survey Telescope for Astronomy (VISTA), operated by the European Southern Observatory (ESO). The data were processed by the Cambridge Astronomical Survey Unit (CASU) and are publicly available through the VISTA Science Archive (VSA; N. J. G. Cross et al. 2012), hosted by the Wide Field Astronomy Unit (WFAU) in Edinburgh. We acknowledge the use of data products from the Wide-field Infrared Survey Explorer, which is a joint project of the University of California, Los Angeles, and the Jet Propulsion Laboratory/California Institute of Technology, and NEOWISE which is a project of the Jet Propulsion Laboratory/California Institute of Technology. WISE and NEOWISE are funded by the National Aeronautics and Space Administration. This research has made use of the SIMBAD database (M. Wenger et al. 2000), the CDS VizieR catalog access tool (F. Ochsenbein et al. 2000), and NASA's Astrophysics Data System (ADS) under Cooperative Agreement 80NSSC21M00561. We further acknowledge the Python programming language and its scientific ecosystem for enabling data analysis and visualization. This work used the following libraries: Astropy (Astropy Collaboration et al. 2013, 2018; Astropy Collaboration et al. 2022), NumPy (C. R. Harris et al. 2020), Matplotlib (J. D. Hunter 2007), and SciPy (P. Virtanen et al. 2020), as well as the `Euclid_tools` (F. Kiwy 2025) Python package for retrieving, inspecting, and classifying Euclid spectral data. During the preparation of this work, the author used ChatGPT to improve the readability and language of the manuscript.

Appendix A
Spectral Characteristics of Candidates

In the following, we describe the spectral characteristics of each candidate, focusing on their alignment with the Burgasser templates (Figure 2) and the reliability of their classifications. The spectral types listed in parentheses after each object name correspond to those inferred from the Burgasser templates; the final adopted spectral types, obtained as the mean of the Burgasser and Theissen classifications, are summarized in Table 5.

E0322−2650 (T7). Elevated noise is present across the full wavelength range of the spectrum. While the *J*-band peak aligns reasonably well with the T7 standard, the *H*-band peak appears slightly elevated relative to the template. The flux within the *J*-band methane and water absorption troughs is somewhat lower than that of the T7 standard. Despite these discrepancies, the overall spectral morphology remains consistent with that of a late T dwarf.

E0328−2749 (T4). Originally reported as a T6 by C. Dominguez-Tagle et al. (2025) and noted as peculiar in M. Žerjal et al. (2025), this object shows a moderately noisy spectrum with noticeable scatter in the *J*-band peak. Similar to E0322−2650, it exhibits an elevated *H*-band peak; however, the overall spectral shape remains well defined. Although the flux values between 1.3 and 1.6 μm are flagged as problematic (orange line), the spectrum still captures the essential features of a mid T dwarf.

E0329−2901 (T2). Previously classified as a T4 by C. Dominguez-Tagle et al. (2025), this spectrum shows clear signatures of an early T dwarf despite moderate noise. Comparable to E0328−2749, the spectrum shows elevated flux in the *H* band relative to the standard, along with increased scatter in the *J*-band peak. Nonetheless, the overall spectral shape remains broadly consistent with our T2 classification.

E0331−2618 (T4). Despite the elevated noise, the spectrum of this object—classified as T5 by C. Dominguez-Tagle et al. (2025)—shows good overall agreement with the T4 template. The *J*-band peak is well defined, and the *H* band displays a clear methane absorption feature. Overall, the spectral morphology is consistent with a mid-T classification, though the noise level introduces some uncertainty in the subtype assignment.

E0331−2725 (T4). This spectrum is notably noisy, which limits the precision of the spectral classification. While the *J*-band peak is reasonably well aligned with the T4 standard, significant deviations are observed in the methane and water absorption features. The *J*-band water absorption trough shows excess flux relative to the template, whereas the *H*-band methane trough dips well below the expected level. Additionally, the *H*-band peak is also not well defined. These discrepancies warrant caution in interpreting the spectral type.

E0331−2712 (T4). Substantial uncertainty across the entire wavelength range affects the reliability of this spectrum. The *J*-band peak near 1.3 μm appears elevated relative to the T4 standard. The *H*-band peak and methane absorption trough also show deviations from the template, likely due to the low S/N. Despite these limitations, the overall spectral morphology is broadly consistent with a mid T dwarf classification, although the precise subtype should be interpreted with caution.

E0348−5016 (T3). This object has been reported by M. Žerjal et al. (2025) as a T dwarf without a specific subtype. Its spectrum is among the cleaner examples in the sample, although the *J*-band peak shows some scatter. Between 1.33 and 1.5 μm, the observed flux slightly exceeds that of the T3 template. Beyond 1.5 μm, the spectrum closely follows the expected shape for a T3 dwarf, with a decently aligned *H*-band peak and trough. Overall, the fit is acceptable, supporting the assigned spectral type.

E0352−4910 (T6). This object was previously identified as a T7 by both J. Y. Zhang et al. (2024) and C. Dominguez-Tagle et al. (2025). Its spectrum is clean and smooth throughout, with low noise and a stable continuum across the full wavelength range. It closely matches the T6 template, with particularly well-aligned methane and water absorption features. A slightly elevated *H*-band peak suggests a marginally later subtype

(T7–T8), but the overall morphology supports a confident mid-to-late T classification.

E0359−4740 (T4). Reported as a T8 dwarf by J. Y. Zhang et al. (2024) and as T7 by C. Dominguez-Tagle et al. (2025), this source exhibits a relatively smooth spectrum despite modest scatter in the *H*-band absorption troughs. Both the *J*- and *H*-band peaks appear elevated relative to the T4 standard, though the water absorption troughs between these peaks align well with the template. Given the discrepancies in peak amplitudes, the T4 classification should be considered with caution.

E0403−4725 (T5). The spectrum exhibits moderate noise throughout, which impacts the clarity of key features. Notable deviations from the T5 template are observed, particularly in the *J*-band absorption troughs, where the flux differs from the expected morphology. Although the overall structure is broadly consistent with a mid T dwarf, the limited spectral quality constrains the precision of the type assignment.

E0404−4639 (T4). This is one of the noisiest spectra in the sample, with a significantly degraded signal in both the *J*- and *H*-band regions. The *J*-band peak aligns reasonably well with the T4 standard, but the absorption features between 1.3 and 1.5 μm fall slightly below the expected flux level. Additionally, the *H*-band peak and trough are poorly defined, likely due to the low S/N. While the overall shape is not inconsistent with a mid T dwarf, the high noise level reduces confidence in the T4 classification, which should be considered tentative.

E0418−4804 (T6). Despite a relatively noisy continuum, the overall spectral morphology is broadly consistent with the T6 standard. The *J*-band peak is clearly defined, though slightly broader than in the template. A noticeable flux deficit is present between 1.6 and 1.65 μm, affecting the match in the *H*-band methane absorption feature. Nonetheless, the key features are recognizable, and the classification as a mid-to-late T dwarf is supported, albeit with moderate confidence.

E1745+6459 (T4). This object was previously classified as T7 by G. N. Mace et al. (2013) and J. Y. Zhang et al. (2024) and as T6 by C. Dominguez-Tagle et al. (2025). It is among the higher-quality spectra in our sample, showing a strong match to the T4 template. Both the *J*- and *H*-band peaks are well aligned in amplitude and shape, and the overall continuum tracks the standard closely. Minor deviations in the *H*-band methane absorption do not affect the mid-T classification.

E1747+6454 (T2). Despite a noise level only slightly higher than that of E1745+6459, this spectrum shows notable discrepancies with the T2 template. Key spectral regions in the *J* and *H* bands are difficult to interpret due to deviations in both peak amplitude and absorption troughs. While the overall flux trend follows the expected pattern for an early T dwarf, the mismatch in specific features reduces the confidence in the assigned classification.

E1805+6444 (T2). This spectrum exhibits significant noise, particularly in the *J* band, which affects the clarity of key absorption features. The flux in the overlapping region of methane and water absorption within the *J* band is noticeably lower than expected for a T2 dwarf, while the *H*-band peak appears elevated relative to the standard. Although the general spectral morphology aligns with an early-T classification, the combination of noise and discrepancies in diagnostic regions limits confidence in the precise subtype.

Appendix B
Comparison with Theissen Templates

Figure 4 compares the Euclid spectra of our candidates with the Theissen templates, illustrating the quality of the spectral fits and highlighting the dominant molecular absorption features.

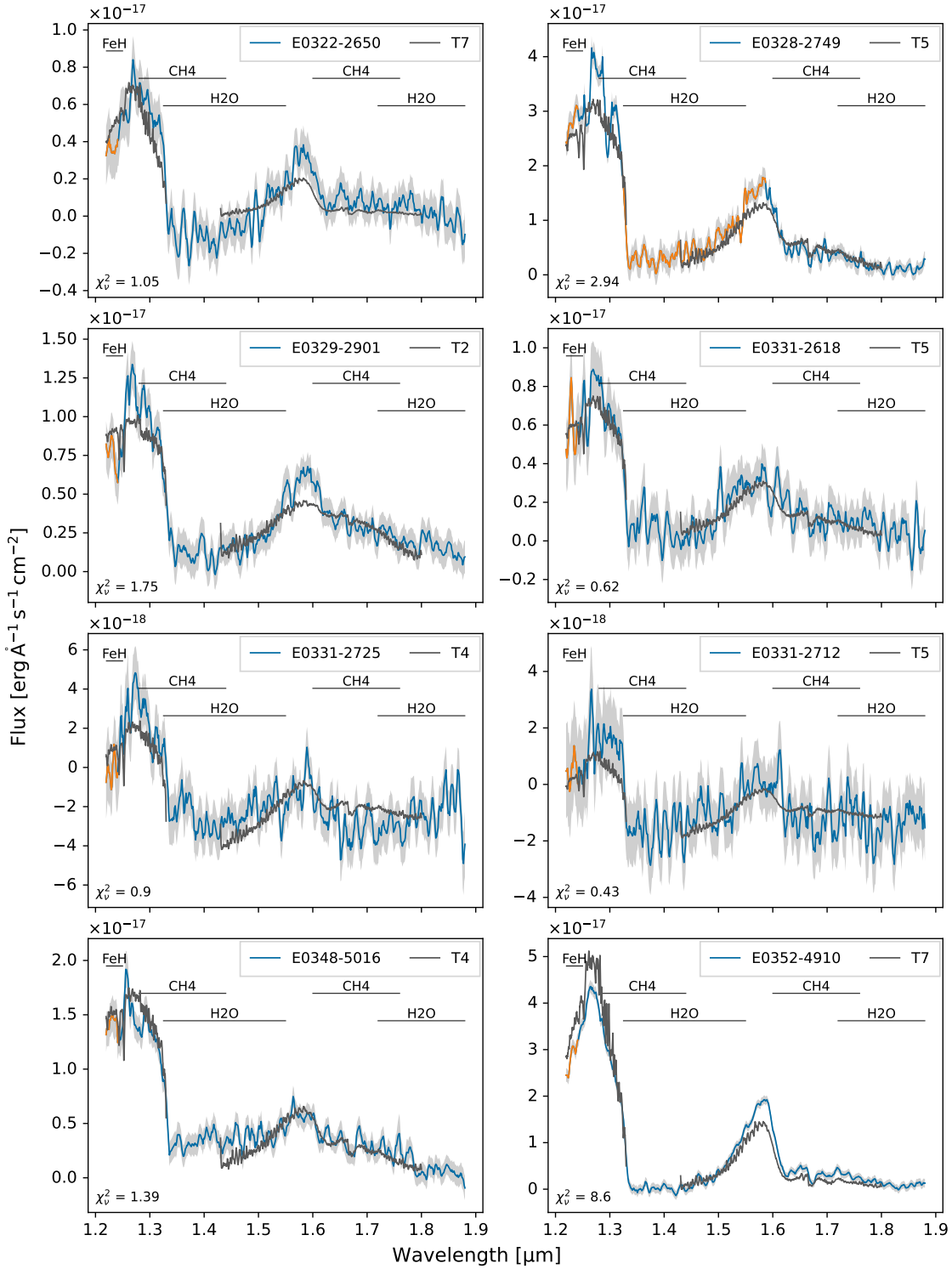

Figure 4. Comparison of smoothed candidate spectra (blue curves) with the Theissen templates (dark gray curves) for the 15 selected candidates. As shown in Figure 2, the orange curves denote flagged values, while the gray shading indicates the flux uncertainty. Key molecular absorption features are marked by horizontal black lines. The inferred spectral types based on the Theissen templates are generally consistent with those derived from the Burgasser templates and agree within one subtype.

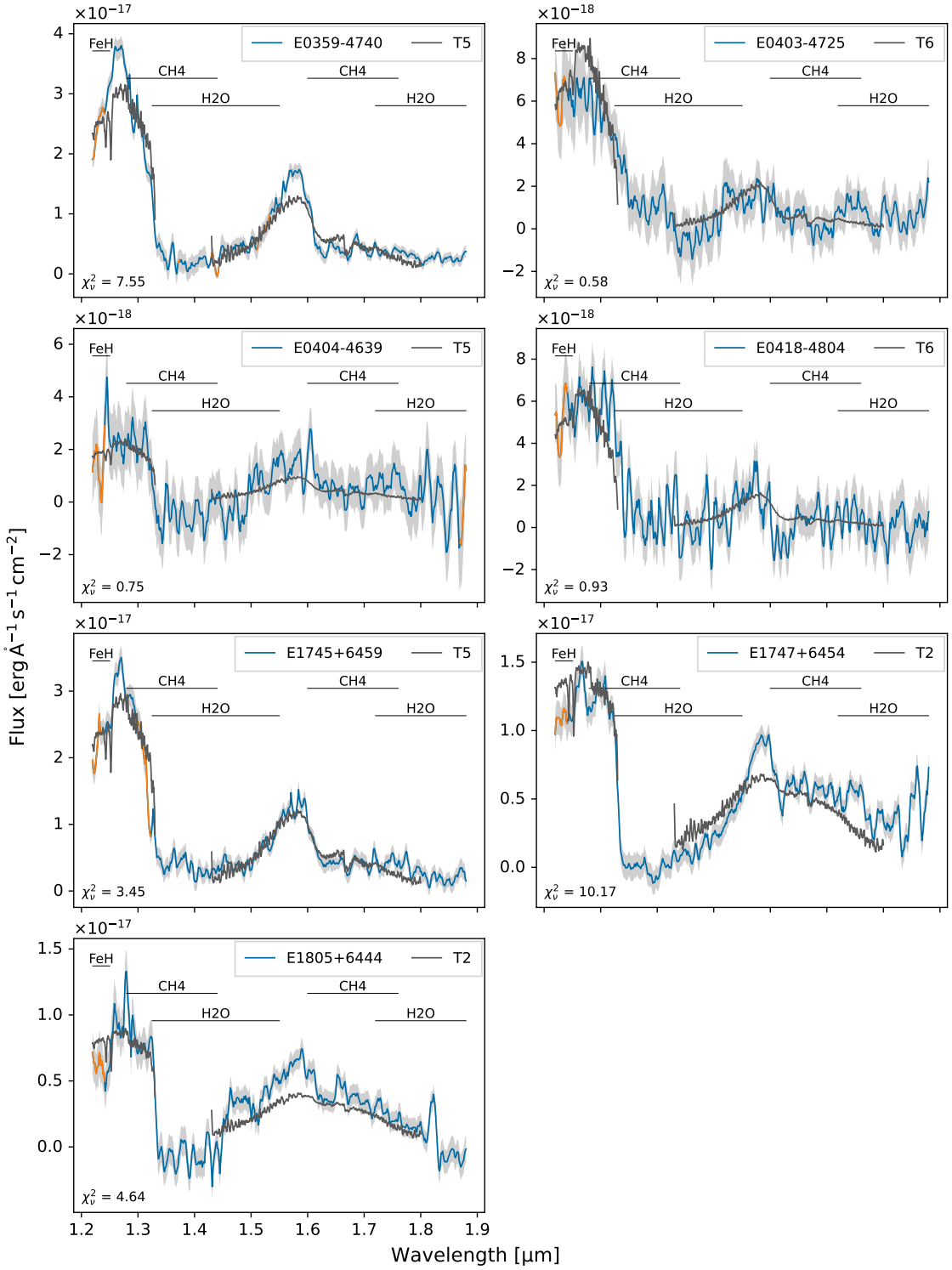

Figure 4. (Continued.)

Appendix C
Synthetic Absolute Magnitudes and Colors

Table 7 lists the synthetic absolute magnitudes and colors from A. Sanghi et al. (2024) adopted in this work and used for the photometric type and distance estimates discussed in the main text.

Table 7
Synthetic Absolute Magnitudes and Colors of Ultracool Dwarfs in the Euclid NISP Bands

SpT	Num. SpT	Age	M_Y (mag)	M_J (mag)	M_H (mag)	$Y-J$ (mag)	$Y-H$ (mag)	$J-H$ (mag)
M6	6	Field	11.634	11.321	11.288	0.313	0.346	0.033
M6	6	Young	10.067	9.804	9.800	0.263	0.267	0.004
M7	7	Field	11.869	11.574	11.480	0.295	0.389	0.094
M7	7	Young	10.912	10.636	10.542	0.276	0.370	0.094
M8	8	Field	12.167	11.851	11.718	0.316	0.449	0.133
M8	8	Young	11.617	11.298	11.141	0.319	0.476	0.157
M9	9	Field	12.522	12.162	11.996	0.360	0.526	0.166
M9	9	Young	12.245	11.859	11.650	0.386	0.595	0.209
L0	10	Field	12.925	12.509	12.305	0.416	0.620	0.204
L0	10	Young	12.835	12.371	12.107	0.464	0.728	0.264
L1	11	Field	13.361	12.887	12.636	0.474	0.725	0.251
L1	11	Young	13.410	12.862	12.535	0.548	0.875	0.327
L2	12	Field	13.813	13.285	12.978	0.528	0.835	0.307
L2	12	Young	13.977	13.348	12.949	0.629	1.028	0.399
L3	13	Field	14.262	13.691	13.320	0.571	0.942	0.371
L3	13	Young	14.531	13.828	13.352	0.703	1.179	0.476
L4	14	Field	14.689	14.088	13.650	0.601	1.039	0.438
L4	14	Young	15.060	14.294	13.741	0.766	1.319	0.553
L5	15	Field	15.077	14.462	13.961	0.615	1.116	0.501
L5	15	Young	15.543	14.731	14.109	0.812	1.434	0.622
L6	16	Field	15.410	14.796	14.244	0.614	1.166	0.552
L6	16	Young	15.959	15.120	14.446	0.839	1.513	0.674
L7	17	Field	15.676	15.078	14.495	0.598	1.181	0.583
L7	17	Young	16.290	15.440	14.742	0.850	1.548	0.698
L8	18	Field	15.869	15.299	14.712	0.570	1.157	0.587
L8	18	Young	16.517	15.674	14.989	0.843	1.528	0.685
L9	19	Field	15.988	15.458	14.899	0.530	1.089	0.559
L9	19	Young	16.632	15.812	15.181	0.820	1.451	0.631
T0	20	Field	16.042	15.557	15.062	0.485	0.980	0.495
T0	20	Young	16.636	15.851	15.322	0.785	1.314	0.529
T1	21	Field	16.046	15.610	15.215	0.436	0.831	0.395
T1	21	Young	16.543	15.800	15.420	0.743	1.123	0.380
T2	22	Field	16.027	15.638	15.378	0.389	0.649	0.260
T2	22	Young	16.385	15.683	15.497	0.702	0.888	0.186
T3	23	Field	16.023	15.678	15.576	0.345	0.447	0.102
T3	23	Young	16.213	15.543	15.586	0.670	0.627	−0.043
T4	24	Field	16.087	15.775	15.843	0.312	0.244	−0.068
T4	24	Young	16.099	15.444	15.734	0.655	0.365	−0.290
T5	25	Field	16.282	15.993	16.221	0.289	0.061	−0.228
T5	25	Young	16.144	15.473	16.007	0.671	0.137	−0.534
T6	26	Field	16.691	16.409	16.763	0.282	−0.072	−0.354
T6	26	Young	16.478	15.747	16.488	0.731	−0.010	−0.741
T7	27	Field	17.411	17.120	17.529	0.291	−0.118	−0.409
T7	27	Young	17.261	16.411	17.284	0.850	−0.023	−0.873
T8	28	Field	18.559	18.240	18.590	0.319	−0.031	−0.350
T8	28	Young	18.692	17.646	18.523	1.046	0.169	−0.877
T9	29	Field	20.270	19.906	20.030	0.364	0.240	−0.124
T9	29	Young	21.004	19.667	20.360	1.337	0.644	−0.693

Note. Synthetic absolute magnitudes (M_Y, M_J, M_H) and colors ($Y-J$, $Y-H$, $J-H$) in the AB magnitude system for spectral types M6–T9 in the Euclid photometric system. These values are derived from the polynomial relations of A. Sanghi et al. (2024) and are provided separately for field-age and young-age populations. Spectral types are listed in both standard notation (SpT) and as numerical codes (Num. SpT). The synthetic sequences are used in our analysis for photometric type and distance estimations of the candidate brown dwarfs.

Appendix D
Detections in Other Surveys

Table 8 summarizes detections of our candidates in complementary surveys, providing additional context on their multiwavelength properties and observational coverage.

Table 8
Near- and Mid-infrared Photometry from VHS, VIKING, and CatWISE2020 for Detected Candidates

Object	Survey	Near-infrared photometry					Mid-infrared photometry			
		z (mag)	Y (mag)	J (mag)	H (mag)	K_s (mag)	W1 (mag)	W2 (mag)	W1 − W2 (mag)	Type
E0328−2749	VIKING	22.041 ± 0.169	19.255 ± 0.034	17.839 ± 0.015	18.167 ± 0.053	17.872 ± 0.066	17.527 ± 0.078	16.228 ± 0.068	1.299	T4
E0329−2901	VIKING	…	20.714 ± 0.101	19.311 ± 0.051	19.446 ± 0.161	18.966 ± 0.167	…	…	…	…
E0331−2618	VHS	…	…	19.798 ± 0.168	…	…	…	…	…	…
E0331−2725	VIKING	…	…	20.758 ± 0.194	…	…	…	…	…	…
E0331−2712	VIKING	…	21.712 ± 0.278	20.615 ± 0.171	…	…	…	…	…	…
E0348−5016	VHS	…	…	18.962 ± 0.078	18.893 ± 0.162	…	…	…	…	…
E0352−4910	VHS	…	…	17.832 ± 0.036	18.218 ± 0.123	18.170 ± 0.169	17.395 ± 0.051	15.264 ± 0.024	2.131	T6
E0359−4740	VHS	…	…	18.073 ± 0.031	18.291 ± 0.062	18.508 ± 0.188	17.231 ± 0.051	15.267 ± 0.027	1.964	T5
E0403−4725	VHS	…	…	19.985 ± 0.146	…	…	…	…	…	…
E0404−4639	VHS	…	…	20.266 ± 0.183	…	…	…	…	…	…
E0418−4804	VHS	…	…	20.215 ± 0.208	…	…	…	…	…	…
E1745+6459	…	…	…	…	…	…	18.032 ± 0.050	16.240 ± 0.033	1.792	T5
E1747+6454	…	…	…	…	…	…	18.325 ± 0.058	16.861 ± 0.040	1.464	T4
E1805+6444	…	…	…	…	…	…	19.004 ± 0.083	17.453 ± 0.056	1.551	T4

Note. VHS (DR7) and VIKING (DR5) $zYJHK_s$ photometry is reported where available, supplemented by CatWISE2020 mid-infrared W1 and W2 measurements. W1 − W2 colors are used to infer photometric types based on the empirical relations of W. M. J. Best et al. (2018), generally consistent with our adopted spectral classifications listed in Table 5. All magnitudes are on the Vega system. Missing values are indicated by an ellipsis.

ORCID iDs

Frank Kiwy https://orcid.org/0000-0001-8662-1622
J. Davy Kirkpatrick https://orcid.org/0000-0003-4269-260X
Adam C. Schneider https://orcid.org/0000-0002-6294-5937
Aaron M. Meisner https://orcid.org/0000-0002-1125-7384
Jacqueline K. Faherty https://orcid.org/0000-0001-6251-0573
Marc J. Kuchner https://orcid.org/0000-0002-2387-5489
Daniella Bardalez Gagliuffi https://orcid.org/0000-0001-8170-7072
Sarah L. Casewell https://orcid.org/0000-0003-2478-0120
Thomas P. Bickle https://orcid.org/0000-0003-2235-761X

References

Astropy Collaboration, Price-Whelan, A. M., Sipőcz, B. M., et al. 2018, AJ, 156, 123
Astropy Collaboration, Price-Whelan, A. M., Lim, P. L., et al. 2022, ApJ, 935, 167
Astropy Collaboration, Robitaille, T. P., Tollerud, E. J., et al. 2013, A&A, 558, A33
Baraffe, I., Chabrier, G., Barman, T. S., Allard, F., & Hauschildt, P. H. 2003, A&A, 402, 701
Beiler, S. A., Cushing, M. C., Kirkpatrick, J. D., et al. 2024, ApJ, 973, 107
Best, W. M. J., Magnier, E. A., Liu, M. C., et al. 2018, ApJS, 234, 1
Best, W. M. J., Sanghi, A., Liu, M. C., Magnier, E. A., & Dupuy, T. J. 2024, ApJ, 967, 115
Buenzli, E., Apai, D., Morley, C. V., et al. 2012, ApJL, 760, L31
Burgasser, A. J. 2007, ApJ, 659, 655
Burgasser, A. J., Cruz, K. L., Cushing, M., et al. 2010a, ApJ, 710, 1142
Burgasser, A. J., Geballe, T. R., Leggett, S. K., Kirkpatrick, J. D., & Golimowski, D. A. 2006, ApJ, 637, 1067
Burgasser, A. J. & Splat Development Team 2017, ASIC, 14, 7
Burgasser, A. J., Kirkpatrick, J. D., Brown, M. E., et al. 2002, ApJ, 564, 421
Burgasser, A. J., Simcoe, R. A., Bochanski, J. J., et al. 2010b, ApJ, 725, 1405
Burgasser, A. J., Schneider, A. C., Meisner, A. M., et al. 2025, ApJ, 982, 79
Burrows, A., Hubbard, W. B., Lunine, J. I., & Liebert, J. 2001, RvMP, 73, 719
Chabrier, G., Baraffe, I., Allard, F., & Hauschildt, P. H. 2005, arXiv:astro-ph/0509798
Chambers, K. C., Magnier, E. A., Metcalfe, N., et al. 2016, arXiv:1612.05560
Chen, A. Y. A., Goto, T., Wu, C. K. W., et al. 2025, PASA, 42, e042
Chen, X., Biller, B. A., Vos, J. M., et al. 2024, MNRAS, 533, 3114
Cross, N. J. G., Collins, R. S., Mann, R. G., et al. 2012, A&A, 548, A119
Cushing, M. C., Marley, M. S., Saumon, D., et al. 2008, ApJ, 678, 1372
Cushing, M. C., Kirkpatrick, J. D., Gelino, C. R., et al. 2011, ApJ, 743, 50
Cutri, R. M., Skrutskie, M. F., van Dyk, S., et al. 2003, IRSA 2MASS All-Sky Point Source Catalog (NASA/IPAC)
Dieterich, S. B., Weinberger, A. J., Boss, A. P., et al. 2018, ApJ, 865, 28
Dominguez-Tagle, C., Žerjal, M., Sedighi, N., et al. 2025, ApJ, 991, 84
Edge, A., Sutherland, W., Kuijken, K., et al. 2013, Msngr, 154, 32
Euclid Collaboration, Jahnke, K., Gillard, W., et al. 2025a, A&A, 697, A3
Euclid Collaboration, Aussel, H., Tereno, I., et al. 2025b, arXiv:2503.15302
Euclid Collaboration, Cropper, M. S., Al-Bahlawan, A., et al. 2025c, A&A, 697, A2
Euclid Collaboration, Romelli, E., Kümmel, M., et al. 2025d, arXiv:2503.15305
European Space AgencyEuclid Consortium 2025, Euclid Quick Release (Q1), European Space Agency
Faherty, J. K., Burningham, B., Gagné, J., et al. 2024, Natur, 628, 511
Faherty, J. K., Meisner, A. M., Burningham, B., et al. 2025, Natur, 645, 62
Gaia Collaboration, Prusti, T., de Bruijne, J. H. J., et al. 2016, A&A, 595, A1
Gardner, J. P., Mather, J. C., Clampin, M., et al. 2006, SSRv, 123, 485
Grieves, N., Bouchy, F., Lendl, M., et al. 2021, A&A, 652, A127
Hainline, K. N., Helton, J. M., Johnson, B. D., et al. 2024, ApJ, 964, 66
Harris, C. R., Millman, K. J., van der Walt, S. J., et al. 2020, Natur, 585, 357
Hubbard, W. B., Guillot, T., Lunine, J. I., et al. 1997, PhPl, 4, 2011
Hunter, J. D. 2007, CSE, 9, 90
Huston, M. J., & Luhman, K. L. 2021, AJ, 161, 138
Kirkpatrick, J. D., Reid, I. N., Liebert, J., et al. 1999, ApJ, 519, 802
Kirkpatrick, J. D., Gelino, C. R., Cushing, M. C., et al. 2012, ApJ, 753, 156
Kirkpatrick, J. D., Gelino, C. R., Faherty, J. K., et al. 2021, ApJS, 253, 7
Kirkpatrick, J. D., Looper, D. L., Burgasser, A. J., et al. 2010, ApJS, 190, 100
Kirkpatrick, J. D., Marocco, F., Gelino, C. R., et al. 2024, ApJS, 271, 55
Kiwy, F. 2025, Euclid_tools v1.0.0, Zenodo:10.5281/zenodo.17846221
Laureijs, R. J., Duvet, L., Escudero Sanz, I., et al. 2010, SPIE, 7731, 77311H
Lawrence, A., Warren, S. J., Almaini, O., et al. 2007, MNRAS, 379, 1599
Line, M. R., Marley, M. S., Liu, M. C., et al. 2017, ApJ, 848, 83
Line, M. R., Teske, J., Burningham, B., Fortney, J. J., & Marley, M. S. 2015, ApJ, 807, 183
Luhman, K. L., Rieke, G. H., Young, E. T., et al. 2000, ApJ, 540, 1016
Mace, G. N., Kirkpatrick, J. D., Cushing, M. C., et al. 2013, ApJS, 205, 6
Marley, M. S., Saumon, D., & Goldblatt, C. 2010, ApJL, 723, L117
Marocco, F., Eisenhardt, P. R. M., Fowler, J. W., et al. 2021, ApJS, 253, 8
Martin, E. C., Mace, G. N., McLean, I. S., et al. 2017, ApJ, 838, 73
McLean, I. S., McGovern, M. R., Burgasser, A. J., et al. 2003, ApJ, 596, 561
McLean, I. S., Prato, L., McGovern, M. R., et al. 2007, ApJ, 658, 1217
McMahon, R. G., Banerji, M., Gonzalez, E., et al. 2013, Msngr, 154, 35
Metchev, S. A., Heinze, A., Apai, D., et al. 2015, ApJ, 799, 154
Miles, B. E., Skemer, A. J. I., Morley, C. V., et al. 2020, AJ, 160, 63
Mohandasan, A., Smart, R. L., Reylé, C., et al. 2025, arXiv:2503.22559
Moraux, E., Bouvier, J., Stauffer, J. R., & Cuillandre, J. C. 2003, A&A, 400, 891
Ochsenbein, F., Bauer, P., & Marcout, J. 2000, A&AS, 143, 23
Radigan, J., Jayawardhana, R., Lafrenière, D., et al. 2012, ApJ, 750, 105
Sanghi, A., Liu, M. C., Dupuy, T. J., et al. 2024, RNAAS, 8, 137
Skrutskie, M. F., Cutri, R. M., Stiening, R., et al. 2006, AJ, 131, 1163
Spiegel, D. S., Burrows, A., & Milsom, J. A. 2011, ApJ, 727, 57
Suárez, G., Faherty, J. K., Burningham, B., et al. 2025, ApJ, 993, 165
Theissen, C. A., Burgasser, A. J., Martin, E. C., et al. 2022, RNAAS, 6, 151
Turner, S. K., Stephens, D. C., Scoresby, C. B., & Miller, J. A. 2025, AJ, 170, 43
Virtanen, P., Gommers, R., Oliphant, T. E., et al. 2020, NatMe, 17, 261
Viscasillas Vázquez, C., Solano, E., Ulla, A., et al. 2024, A&A, 691, A223
Vos, J. M., Burningham, B., Faherty, J. K., et al. 2023, ApJ, 944, 138
Wenger, M., Ochsenbein, F., Egret, D., et al. 2000, A&AS, 143, 9
Werner, M. W., Roellig, T. L., Low, F. J., et al. 2004, ApJS, 154, 1
Wright, E. L., Eisenhardt, P. R. M., Mainzer, A. K., et al. 2010, AJ, 140, 1868
Yamamura, I., Tsuji, T., & Tanabé, T. 2010, ApJ, 722, 682
Yang, M., Zhang, B., Jiang, B., et al. 2024, ApJ, 965, 106
York, D. G., Adelman, J., Anderson, J. E., Jr., et al. 2000, AJ, 120, 1579
Zahnle, K. J., & Marley, M. S. 2014, ApJ, 797, 41
Zhang, J. Y., Lodieu, N., & Martín, E. L. 2024, A&A, 686, A171
Zhang, Z., & Li, Y. 2025, AJ, 170, 360
Žerjal, M., Dominguez-Tagle, C., Sedighi, N., et al. 2025, arXiv:2503.22497